Journal of Applied Physics

Variations of light emission and carrier dynamics around V-defects in InGaN quantum wells

Cite as: J. Appl. Phys. **128**, 225703 (2020); https://doi.org/10.1063/5.0031863
Submitted: 04 October 2020 . Accepted: 19 November 2020 . Published Online: 09 December 2020

Rinat Yapparov, Yi Chao Chow, Cheyenne Lynsky, Feng Wu, Shuji Nakamura, James S. Speck, Saulius Marcinkevičius, et al.

View Online Export Citation CrossMark

ARTICLES YOU MAY BE INTERESTED IN

Effect of AlGaN interlayer on the GaN/InGaN/GaN/AlGaN multi-quantum wells structural properties toward red light emission
Journal of Applied Physics **128**, 223102 (2020); https://doi.org/10.1063/5.0027119

A 3D simulation comparison of carrier transport in green and blue c-plane multi-quantum well nitride light emitting diodes
Journal of Applied Physics **128**, 235703 (2020); https://doi.org/10.1063/1.5143276

Comparison of size-dependent characteristics of blue and green InGaN microLEDs down to 1 μm in diameter
Applied Physics Letters **116**, 071102 (2020); https://doi.org/10.1063/1.5144819

HIDEN ANALYTICAL Instruments for **Advanced Science**

- Knowledge,
- Experience,
- Expertise

Click to view our product catalogue

Contact Hiden Analytical for further details:
W www.HidenAnalytical.com
E info@hiden.co.uk

Gas Analysis
- dynamic measurement of reaction gas streams
- catalysis and thermal analysis
- molecular beam studies
- dissolved species probes
- fermentation, environmental and ecological studies

Surface Science
- UHV TPD
- SIMS
- end point detection in ion beam etch
- elemental imaging - surface mapping

Plasma Diagnostics
- plasma source characterization
- etch and deposition process reaction kinetic studies
- analysis of neutral and radical species

Vacuum Analysis
- partial pressure measurement and control of process gases
- reactive sputter process control
- vacuum diagnostics
- vacuum coating process monitoring

© 2020 Author(s).

Journal of
Applied Physics

ARTICLE

scitation.org/journal/jap

Variations of light emission and carrier dynamics around V-defects in InGaN quantum wells

Cite as: J. Appl. Phys. **128**, 225703 (2020); doi: 10.1063/5.0031863
Submitted: 4 October 2020 · Accepted: 19 November 2020 ·
Published Online: 9 December 2020

View Online Export Citation CrossMark

Rinat Yapparov,[1] Yi Chao Chow,[2] Cheyenne Lynsky,[2] Feng Wu,[2] Shuji Nakamura,[2] James S. Speck,[2] and Saulius Marcinkevičius[1,a)]

AFFILIATIONS

[1] Department of Applied Physics, KTH Royal Institute of Technology, AlbaNova University Center, 10691 Stockholm, Sweden
[2] Materials Department, University of California, Santa Barbara, California 93106, USA

[a)] **Author to whom correspondence should be addressed:** sm@kth.se

ABSTRACT

Time- and spectrally-resolved scanning near-field optical microscopy was applied to study spatial variations of photoluminescence (PL) spectra and carrier dynamics in polar InGaN/GaN single quantum wells (QWs) emitting from 410 nm to 570 nm. The main attention was devoted to variations of PL properties and carrier dynamics around V-defects. The PL intensity, peak wavelength, and linewidth, as well as the radiative and nonradiative recombination times, were found to be different in V-defect-rich and defect-free regions. The radiative lifetime close to the defects was longer up to several times, which is attributed to an increased electron and hole wave function separation in the QW plane. PL decay times, measured using excitation and collection through the near-field probe, were one to two orders of magnitude shorter than PL decay times measured in the far field. This shows that the near-field PL decay and the integrated PL intensity are primarily determined by the carrier out-diffusion from under the probe. Only in the immediate vicinity of the V-defects, the near-field PL decays due to the nonradiative recombination at dislocations. The area of such enhanced nonradiative recombination is limited to just a few percent of the total QW area. This shows that recombination via dislocations and V-defects does not play a decisive role in the overall nonradiative recombination and internal quantum efficiency of polar InGaN/GaN QWs.

I. INTRODUCTION

One of the most striking features of InGaN/GaN quantum well (QW) light emitting diodes is their high brightness. Despite the large ($\sim 10^8$ cm^{-2}) density of dislocations in polar *c*-plane device structures heteroepitaxially grown on foreign substrates, the external quantum efficiency of state of the art violet and blue light emitting diodes (LEDs) at low currents is about 90%.[1] Several mechanisms have been proposed to explain this peculiar phenomenon. The first one is carrier localization at band potential fluctuations that prevents the nonradiative recombination. The band potential fluctuations may be induced by InGaN alloy composition[2] and QW width[3] variations with the alloy composition probably playing the main role.[4] The second mechanism is the formation of potential barriers around dislocations that prevent carrier capture into dislocation-related nonradiative recombination centers.[5] The origin of these barriers has been assigned to thin semipolar QWs present on $\{10\bar{1}1\}$ facets of V-defects (sometimes referred to as V-pits).[5] The V-defects form at threading dislocations and/or In-rich clusters and have a shape of inverted hexagonal pyramids.[6]

While research efforts historically focused on minimizing V-defects in III-nitride LEDs because they were considered detrimental to the device performance, recent studies indicate that V-defects may have a positive impact on the efficiency of LEDs, especially those operating at long wavelengths. Apart from the mentioned potential barriers around the dislocations that prevent the nonradiative recombination, it has been suggested that V-defects can improve LED efficiency by enhancing hole injection into deep *c*-plane QWs via the semipolar sidewall QWs.[7]

The V-defects nucleate as a result of surface depressions caused by threading dislocations and grow due to kinetically limited growth.[6] Increasing either the In content or period of InGaN/GaN layers in superlattices or multiple QWs has been found to promote V-defect growth.[6,8] Thus, V-defect formation can be controlled by adjusting growth conditions and structure parameters. An impact of the engineered V-defects on the wall plug efficiency of long-wavelength InGaN/GaN LEDs has been demonstrated by Jiang *et al.* and represents an important development in III-nitride photonic devices.[9]

The influence of V-defects on electronic and optical properties of InGaN/GaN QWs is rather complex. For instance, it has been shown that the formation of the V-defects might cause a partial strain relaxation,[10,11] which, in turn, would alter the local InGaN alloy composition.[12] Such local variations of the chemical composition and mechanical properties would influence both electronic and optical properties of the QWs. While spatial variations of the emission spectra have been studied by several groups,[12–22] the impact of the V-defects on the carrier recombination has not yet been addressed.

To explore the local electronic and optical properties around V-defects in QWs, investigations with a high spatial resolution are necessary. Such measurements are typically performed by scanning cathodoluminescence (CL)[12–15] and photoluminescence (PL) using micro-PL[16] or scanning near-field optical microscopy (SNOM) techniques.[5,17–22] The latter method, for instance, has been used to identify the potential barriers caused by the sidewall semipolar QWs.[5]

In this work, we have used SNOM to study the effect that V-defects have on the local radiative lifetime and PL dynamics. To explore the dependence of these properties on QW depth, InGaN/GaN QWs emitting from 410 nm to 570 nm have been studied. Experiments were performed using a multimode SNOM technique,[23] which allows mapping the radiative and PL decay times along with parameters of PL spectra and surface topography.

II. EXPERIMENTAL DETAILS

The studied samples were InGaN/GaN single QW structures grown by metal-organic chemical vapor deposition on a sapphire substrate. They consisted of a 4 μm thick GaN buffer, a 20 period $In_{0.05}Ga_{0.95}N/GaN$ superlattice, a 50 nm GaN layer, a 3 nm QW, and a 12 nm GaN cap layer. The small thickness of the cap layer was chosen to maintain a good near-field contact between the QW and the near-field probe. The indium content in the wells, evaluated from x-ray diffraction of calibration samples, was 11%, 15%, 19%, and 25% for the violet, blue, green, and green-yellow QWs, respectively. The structures were not intentionally doped. The density of V-defects, estimated from atom force microscopy (AFM) maps [Fig. 1(a)], was 2×10^8 cm^{-2} for all samples. The average area of a V-defect at the surface was 1.3×10^{-10} cm^2. The V-defect formation started in the InGaN/GaN superlattice, which was identical for all samples. Hence, the properties of the V-defects did not depend on the composition of the QW alloy.

Experiments were performed at room temperature with a scanning near-field optical microscope operating in the illumination–collection (I–C) mode (PL excited and collected through the same probe). For excitation, 200 fs pulses from the second (390 nm) and third (260 nm) harmonics of a self-mode-locking Ti:sapphire laser were used. In the first case, carriers were excited only in the QWs; in the second case, the majority of the carriers were generated in the barriers. Maps of time-integrated and time-resolved PL parameters for both excitation regimes were identical showing that carrier transport in the barriers and capture to the QWs did not affect the measurement results. To assure that all photoexcited carriers recombine between the excitation pulses, the laser pulse repetition rate (80 MHz) was reduced to 4 MHz using a pulse picker. Time-integrated PL spectra at each position of a scan were recorded using a spectrometer with a liquid N_2 cooled CCD array detector. Time-resolved PL transients were recorded using a time-correlated single photon counter after selecting QW PL with bandpass filters. Both time-integrated and time-resolved data were taken simultaneously after splitting the PL beam with a beam splitter. The aperture of the Al-coated SNOM probe was about 150 nm. Additional measurements with a large (∼400 nm) aperture probe and in the far field were performed as well. Maps of the surface morphology were recorded using a feedback signal from the tuning fork. For each sample, several scans with areas varying from $4 \times 4 \mu m^2$ to $10 \times 10 \mu m^2$ were made. To evaluate the average radiative and nonradiative recombination times, additional far-field time-resolved PL measurements in the temperature range from 10 to 300 K were carried out.

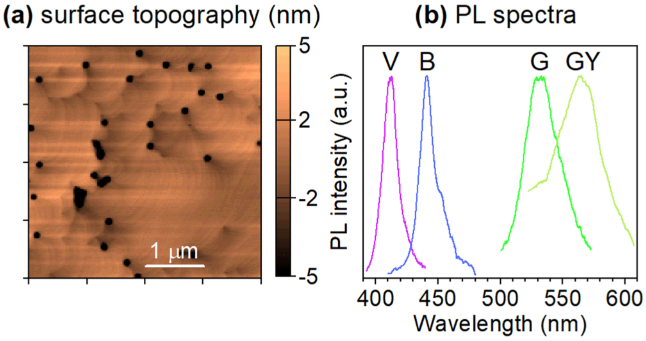

FIG. 1. A typical $5 \times 5 \mu m^2$ AFM scan (a) and representative near-field PL spectra of the studied violet (V), blue (B), green (G), and green-yellow (GY) QWs (b).

Additional studies of the QW width and alloy composition around V-defects and in defect-free areas were performed on a multiple QW structure grown under similar conditions as the single QWs. Experiments were performed using high angle annular dark-field scanning transmission microscopy (HAADF-STEM) and energy-dispersive x-ray spectroscopy (EDS). HAADF images and EDS element maps were acquired using a Talos G2 200× TEM/STEM system equipped with ChemiSTEM EDS, operated at 200 kV.

III. RESULTS

Figure 1(b) shows typical near-field PL spectra for the studied QWs. Figures 2–4 show $4 \times 4 \mu m^2$ maps of different PL parameters for the violet, blue, and green-yellow QWs.

Maps of the surface topography, integrated PL intensity, peak wavelength, and full width at half maximum (FWHM) for the violet QW are presented in Figs. 2(a)–2(d). The PL decay time, determined from a single-exponential fit of the PL decay, is shown in Fig. 2(e). The map of the radiative recombination time, built from the map of inverse transient amplitudes (proportional to the radiative lifetime[23]) and normalized to the average radiative recombination time at room temperature,[24] is presented in Fig. 2(f).

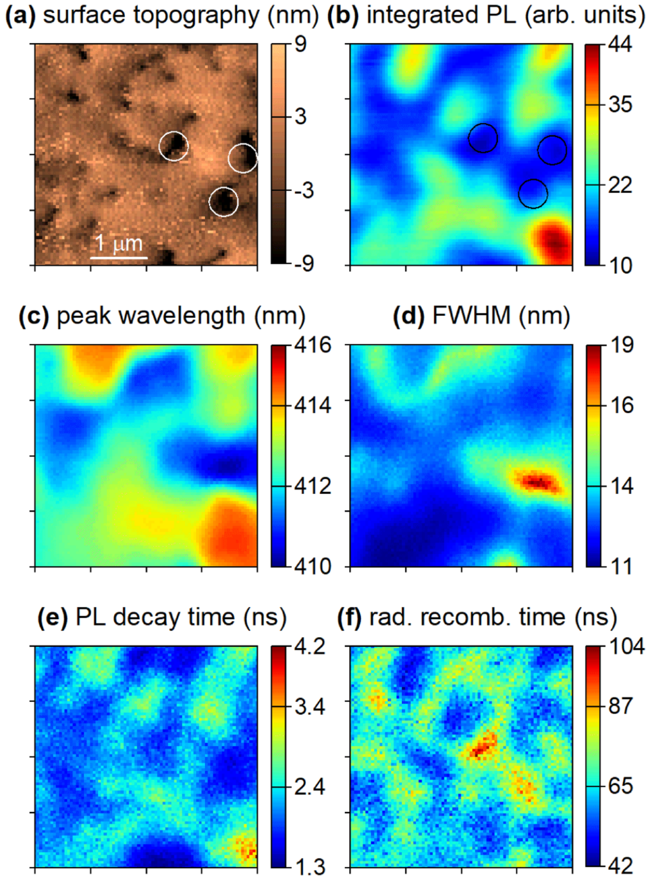

FIG. 2. Maps of the surface topography (a), integrated PL intensity (b), peak wavelength (c), FWHM (d), PL decay time (e), and radiative recombination time (f) for the violet QW. White and black circles in maps (a) and (b) relate several topography features (V-defects and their groups) with their counterparts in the PL intensity map. Note that small, pixel-size (~$50 \times 50\,\text{nm}^2$) features in these and other maps originate from the SNOM tuning fork noise and do not reflect sample properties.

The average radiative lifetime was determined from far-field PL transients measured at different temperatures following the procedure of Ref. 25.

In the surface topography map, one can distinguish regions with single and grouped V-defects. Because of the limited spatial resolution (a SNOM probe is much thicker than a dedicated AFM probe), not all individual V-defects are well resolved [cf. Fig. 1(a)]. However, this low-resolution map is suitable to search for correlations between the topography and optical maps. Here, one should bear in mind that a small shift between the topography and optical maps related to the nature of a metal-coated SNOM probe may occur. While the optical signal is collected through the aperture in the middle of the probe, the topography map might be recorded by an edge of the metal coating.

Visually, correlations between the topography and the PL maps are quite clear. In the regions of major defects and/or their groups, the PL intensity is lower, the peak wavelength is slightly longer, and the FWHM is larger. The spectral PL broadening in the defect regions agrees with the recent confocal microscopy results.[11]

The presented and other PL intensity maps for the violet QW show that spatial PL intensity variations are large with an enhancement in the defect-free regions by as much as five times. Spatial variations of the PL decay time and radiative lifetime are substantial as well. In the V-defect regions, the PL decay time is shorter and the radiative lifetime is longer by several times compared to the defect-free regions. Variations of the radiative lifetime in this *c*-plane QW are considerably larger than in homoepitaxial nonpolar and semipolar InGaN/GaN QWs without V-defects.[4,24]

Corresponding maps for the blue QW are shown in Fig. 3. Correlations between the topography and optical maps, similar to those for the violet QW, are observed. In the V-defect-rich regions, the PL decay time is shorter and the radiative recombination time is longer. The spatial PL intensity and decay time variations are even larger than for the violet QW. Figure 3(d) shows a plot for the correlation between the PL intensity and peak wavelength. These PL parameters strongly correlate with the Pearson product-moment correlation coefficient $r = 0.61$. Areas with a larger PL intensity correspond to regions emitting at longer wavelengths. The complex correlation plot displays several "branches" that reflect different regions of the scan showing that properties of different V-defects and their groups are not identical. The corresponding correlation plot for the violet QW (not shown) is very similar.

Figure 4 shows surface topography and SNOM maps for the green-yellow QW. Contrary to the shorter wavelength QWs, there is no clear correlation between the PL intensity and peak wavelength [Fig. 4(d)]. This is because in the long-wavelength QWs most of the localization sites are deep, and the depth of the potential minima (and the PL wavelength) no longer correlates with the rate of the nonradiative recombination and/or velocity of carrier diffusion. Due to long carrier lifetimes (see Table II) and smaller signal, the lifetime maps are less resolved. Nevertheless, correlations between the surface topography and optical maps can be traced for the green (not shown) and green-yellow QWs as well.

Quantitatively, correlations between the different maps are evaluated using Pearson's correlation coefficients (Table I). The correlations between the topography and optical maps are moderate albeit statistically significant. There are several reasons for the modest correlation coefficient values. First, the morphology and optical maps might be registered with different parts of the near-field probe and with a different spatial resolution. Second, not all defect-rich regions might give identical optical responses, as it is demonstrated in Fig. 3(d). Third, regions between closely spaced V-pits might appear flat in the topography; however, the InGaN alloy composition might strongly vary (see Fig. 7). Nevertheless, the general trends reflected in the correlation coefficients are clear and similar for all the samples, independently of the QW depth.

Plots for the correlations between the surface topography, and PL decay and radiative recombination times for the blue QW are shown in Fig. 5. In the V-defect-rich regions (negative height values), the PL decay time is shorter and the radiative lifetime is longer. The same dependence is observed for all the samples (Table I). The PL decay time and radiative lifetime anti-correlate.

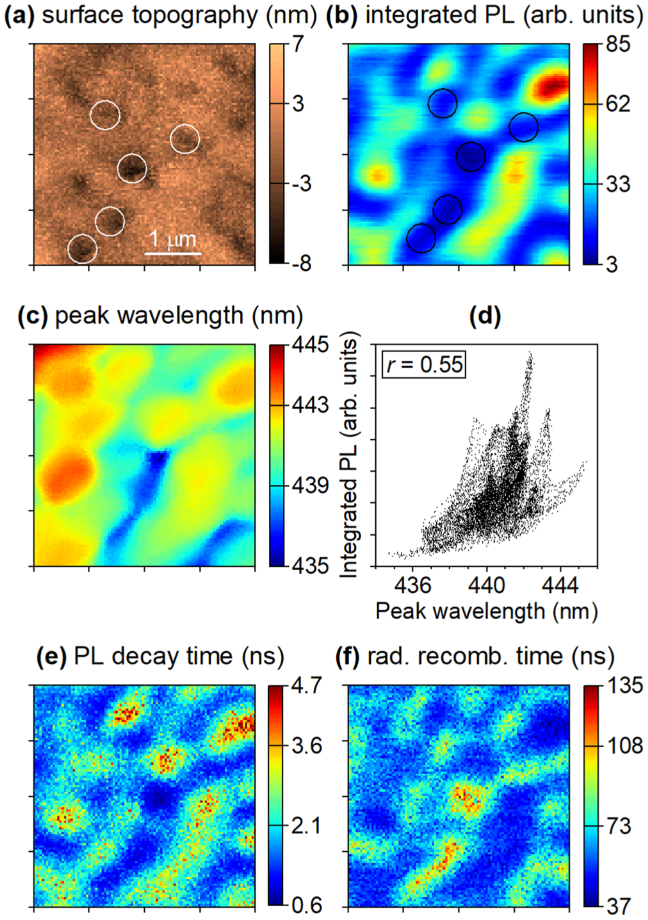

FIG. 3. Maps of the surface topography (a), integrated PL intensity (b), peak wavelength (c), PL decay time (e), and radiative recombination time (f) for the blue QW. Part (d) shows a correlation between the PL peak wavelength and integrated intensity.

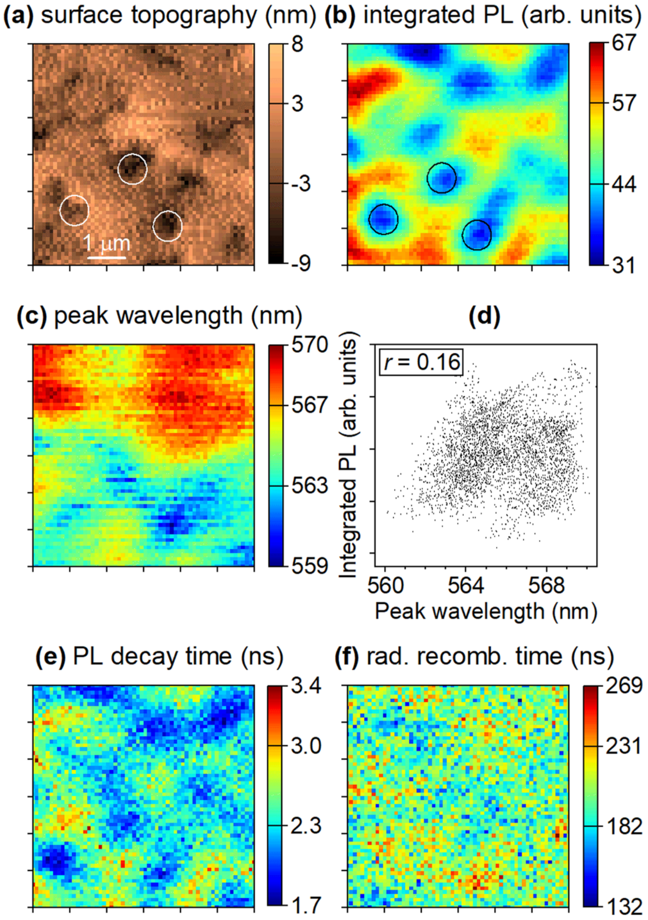

FIG. 4. Maps of the surface topography (a), integrated PL intensity (b), peak wavelength (c), PL decay time (e), and radiative recombination time (f) for the green-yellow QW. Part (d) shows a correlation between the PL peak wavelength and integrated intensity.

This is demonstrated in Fig. 5(c) in which overlapped radiative lifetime and PL decay time maps for the blue QW are shown.

IV. DISCUSSION

A. Radiative recombination time

The radiative lifetime in a QW is determined by the transition matrix element and the integral of electron and hole wave function overlap. The matrix element for the transitions between the ground electron and hole states in a QW may be considered spatially uniform. The overlap, on the other hand, varies. The wave function overlap may be affected by the vertical electron and hole separation across the QW and by the lateral separation in the QW plane (Fig. 6). The vertical wave function separation takes place in polar and semipolar QWs and is caused by an internal electric field induced by the difference of the spontaneous and piezoelectric polarizations in the well and barrier materials.[26] The lateral wave function separation occurs when an electron and a hole are localized at different sites in the QW plane.[3,27] The latter mechanism requires the presence of localization sites and, in the case of optical excitation, spatial separation of photoexcited electrons and holes prior to their localization.[28] The localization sites form at nm-scale band potential fluctuations of the InGaN alloy and/or variations of the QW width and are common to III-nitride QWs. The spatial separation takes place via diffusion and drift of photoexcited carriers. Taking into account the ultrafast photoexcited carrier relaxation in nitrides,[29] the drift induced by local electric fields is expected to be the leading mechanism. The local in-plane electric fields may be induced by polarization charges at nonplanar QW interfaces[28] and by the band potential variations.[30] Below we discuss the role that these effects have on the spatial variations of the radiative lifetimes.

Let us start with the vertical electric field. In InGaN/GaN QWs, the field is dominated by its piezoelectric component;

TABLE I. Pearson product-moment coefficients for correlations between the surface topography and optical maps and between certain optical maps.

Sample	Intensity/ topography	Peak wavelength/ topography	FWHM/ topography	Decay time/ topography	Radiative lifetime/ topography	Intensity/ FWHM
Violet QW	0.41	0.30	−0.41	0.38	−0.40	−0.42
Blue QW	0.55	0.38	−0.40	0.41	−0.52	−0.64
Green QW	0.36	0.41	−0.36	0.45	−0.31	−0.35
Green-yellow QW	0.68	0.47	−0.55	0.46	−0.26	−0.60

e.g., for a 3 nm thick $In_{0.10}Ga_{0.90}N$/GaN QW, which is very similar to our violet QW, the vertical electric field induced by the difference of the spontaneous polarizations is 30 kV/cm, while the piezoelectric field is −1.66 MV/cm,[31] The electric field strength is proportional to the In content in the QW; hence, for longer wavelength QWs, the field is even stronger.[26]

The vertical electric field, generally considered uniform in planar sections of a QW, would experience considerable fluctuations around the V-defects. First, the piezoelectric field would be affected by the partial strain relaxation. In InGaN epilayers, the strain relaxation due to the formation of the V-defects may be large, up to 80%.[9] In addition, the strain relaxation is spatially nonuniform being larger in the regions of defect groups compared to individual defects.[32] In InGaN/GaN QWs, however, the local strain relaxation in the V-defect regions is much smaller, only about 1%.[11] Second, the local piezoelectric field would be influenced by semipolar QWs on the V-defect sidewalls, where the electric field is several times weaker.[33,34] In general, because the semipolar QWs are thinner[5] and might have a lower In content,[35] their emission should be blue-shifted with respect to the *c*-plane QW.[5] However, this feature does not seem to be universal: PL from semipolar QWs spectrally close to the emission from polar QWs has been observed.[36] Thus, to test whether emission from the sidewall QWs could affect our SNOM data, the well width and alloy composition in the vicinity of V-defects were investigated using HAADF-STEM and EDS. Experiments were performed on a multiple QW structure grown under similar conditions and having the same V-defect density as our single QWs.

Figure 7(a) presents the HAADF-STEM image of a V-defect region, and Figs. 7(b) and 7(c) present the EDS maps of the Ga and In atom content. Variations of the cation atomic fractions along the *c*-axis close to the defect and across the semipolar QWs are shown in Fig. 7(d). In the defect-free area (planar QWs), the average In content in the QWs is 22%. In the semipolar QWs, which are on the sidewalls of the V-defect, the In content is less than 10%. In the regions of the *c*-plane QWs surrounding the defects, the In content is increased up to 30% showing that In atoms that are not incorporated into the sidewall QWs segregate around the V-defect. Unfortunately, these composition variations are not resolved in the SNOM peak wavelength maps because of the limited (∼150 nm) spatial resolution. However, they are

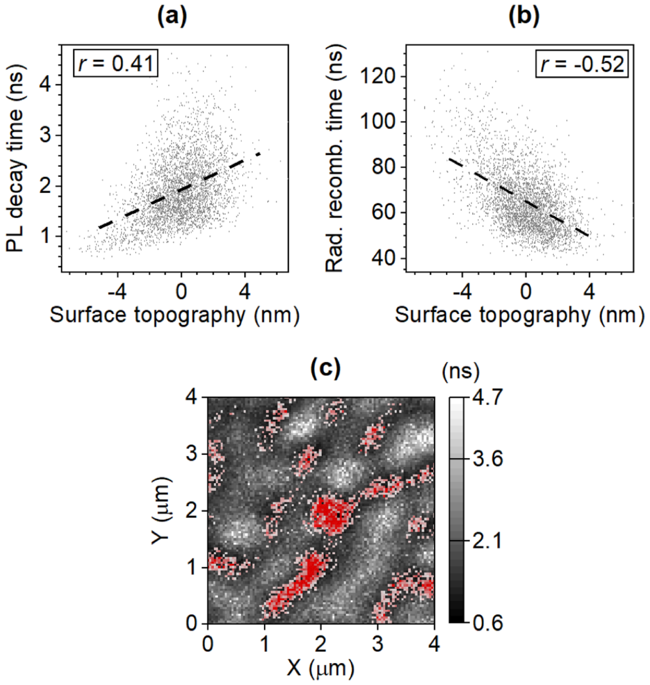

FIG. 5. Correlations between the maps of the PL decay time (a) and radiative lifetime (b) with the surface topography for the blue QW. Plot (c) shows regions with the longest radiative lifetimes (in red) superimposed on the map of the PL decay time.

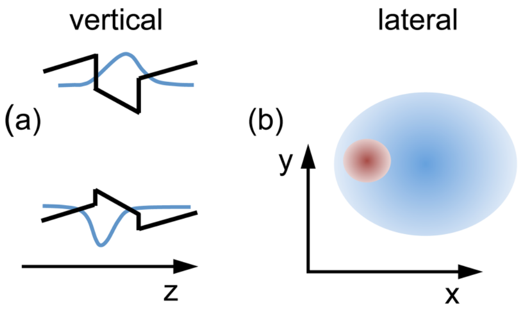

FIG. 6. Schematics illustrating decreased vertical (a) and lateral (b) electron and hole wave function overlap. In part (b), the squared hole wave function is depicted as a small brown circle and the electron wave function is depicted as a large blue ellipse.

TABLE II. PL decay times and radiative lifetimes measured in different configurations.

Sample	Average rad. lifetime (ns)	Minimal rad. lifetime (ns)	Average decay time, small app. (ns)	Minimal decay time, small app. (ns)	Average decay time, large app. (ns)	Decay time, far field (ns)
Violet QW	56	31	2.5	1.3	5	23
Blue QW	60	34	2.4	0.8	9	38
Green QW	175	120	3.3	2.1	16	115
Green-yellow QW	280	210	2.6	1.7	15	153

reflected in the increased FWHM in the defect-rich regions. The HAADF-STEM data also show that the semipolar sidewall QWs are much thinner than the *c*-plane QWs in the defect-free regions. This, in combination with the low In content, shows that emission from the semipolar QWs cannot spectrally overlap with emission from the *c*-plane QWs and affect the SNOM maps. Hence, an increase of the radiative lifetime around the V-defects cannot be assigned to the presence of semipolar sidewall QWs. Neither can it be assigned to the variations of strain. A reduced strain in the defect-rich regions would increase the electron and hole wave function overlap and decrease the radiative lifetime, contrary to the experimental observations.

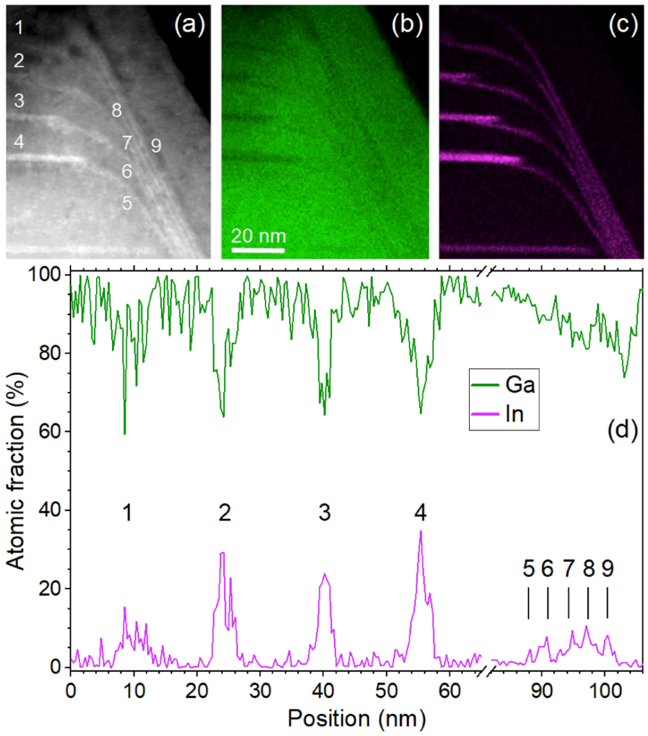

FIG. 7. HAADF-STEM image of a multiple QW structure in the vicinity of a V-defect (a), and EDS images of Ga (b) and In (c) concentrations. Part (d) presents Ga and In profiles around the V-defect. The left hand side shows cation distribution in the c-plane region and the right hand side in the sidewall QW region. The peaks in part (d) correspond to QW numbers in part (a).

The second mechanism that can cause the radiative lifetime variations is the lateral wave function separation due to electron and hole localization at different sites. In the V-defect regions, the luminescence FWHM is typically larger, which indicates a larger inhomogeneous broadening. This increase of the inhomogeneous broadening is induced by the composition variations detected by the EDS (Fig. 6) that are superimposed on the binomial cation distribution in the InGaN QWs.[37]

The inhomogeneous broadening can be evaluated by subtracting the homogeneous broadening (47 meV for InGaN QWs at 300 K, Ref. 38) from the width of the absorption edge or PL linewidth. The absorption spectrum provides a better measure because the PL linewidth might not account for shallow localization minima that are not filled at room temperature. However, at least for InGaN with a low In content (most relevant for the further discussion), the inhomogeneous broadening evaluated from the absorption edge and near-field PL is similar.[39] Hence, in the following, we will use inhomogeneous broadening evaluated from the PL.

Let us first address the violet QW. For its planar sections, the inhomogeneous broadening is 90 meV. To evaluate which part of this broadening takes place in the conduction and which in the valence band, one should consider the depth of the band potential fluctuations and the spread of the carrier wave functions. In general, the band potential fluctuations are larger in the conduction band.[40] However, the electron wave function extends over several potential minima, and the potential landscape seen by an electron is smoothed to about 1/4 of the total inhomogeneous broadening.[40] No such effect is experienced by heavy holes. Thus, for the planar sections of the violet QW, the effective localization depth for electrons is ~23 meV while it is ~67 meV for holes. Such depth of the effective minima in the conduction band is too small to hold the electron localized at room temperature. Hence, the electron would be attracted to and located in the region of a localized hole. In such a case, the lateral wave function separation would be negligible, and the radiative lifetime would be determined by the vertical electron and hole wave function separation. On the other hand, in the defect-rich sections of the violet QW, the inhomogeneous broadening and the effective conduction band potential fluctuations are 120 meV and 30 meV, respectively. The latter value suggests that the electron localization becomes relevant to a larger extent, reducing the in-plane electron and hole wave function overlap and increasing the radiative lifetime.

For the longer wavelength QW, the inhomogeneous broadening is larger, and the lateral separation of electrons and holes takes place in both defect-rich and defect-free regions. Still, around V-defects, the band potential fluctuations are larger, and the related nm-scale in-plane electric fields are stronger. Such fields would contribute to a larger photoexcited electron and hole separation prior to localization, resulting in an increased radiative lifetime.

Apart from the large radiative lifetime variations within the same QWs, one can notice that the average radiative lifetime for different QWs increases with the In content (Table II). This observation is not new: it has been noted for both polar and semipolar QWs and attributed to an increased electron and hole wave function separation by the piezoelectric field.[33] However, as our near-field data show, the local radiative lifetime for a QW with a smaller In content may exceed the local time for a QW with a higher In content. This demonstrates that both the vertical and lateral electron and hole wave function separations are important in defining the local radiative lifetime. In a schematic picture, one can consider that the vertical electric field affects all carriers and defines the average radiative lifetime. The in-plane fields act on the nm-scale and may be different in different parts of a QW inducing small-scale radiative lifetime variations observed by the SNOM.

B. Near-field photoluminescence decay time

The spatial variations of the PL decay time are different from that of the radiative recombination time. In general, in the defect-rich regions, the PL decay time is shorter than in defect-free regions. From the first glance, it would be natural to assign the shorter PL decay times to an enhanced nonradiative recombination. However, for near-field PL decay times measured in the I–C mode, the situation is more complex.

In standard time-resolved far-field measurements, the PL intensity $I(t)$ is independent of the location of radiatively recombining electron–hole pairs (or excitons) with concentration $N(x, y, t)$,

$$I(t) = A \iint_{xy} N(x, y, t) dx dy. \tag{1}$$

Here, A is the product of the measurement transfer function considered to be spatially uniform and the internal quantum efficiency of the sample. The integration takes place over the area in which the electron–hole pairs are present. The PL intensity decays with a time- but not position-dependent decay rate $1/\tau_{PL}(t)$, $dI/dt = AN(t)/\tau_{PL}(t)$. The PL decay rate depends on the radiative and nonradiative recombination rates, $1/\tau_{PL}(t) = 1/\tau_r(t) + 1/\tau_{nr}(t)$. In the I–C mode, the decay time of the local PL intensity also depends on the ambipolar diffusion because the signal is collected only from those electron–hole pairs that radiatively recombine under the probe. The decay of the local electron–hole pair concentration $N(x, y)$ is expressed as[22]

$$\frac{\partial N(x, y, t)}{\partial t} = D_x \frac{\partial^2 N}{\partial x^2} + D_y \frac{\partial^2 N}{\partial y^2} - \frac{N}{\tau_{PL}(x, y)}, \tag{2}$$

where $D_{x(y)}$ are the in-plane components of the ambipolar diffusion tensor. For a c-plane QW, the in-plane diffusion is isotropic, $D_x = D_y$. If the diffusion is slow with a diffusion length smaller than the aperture size, the last term of Eq. (2) dominates, and the PL decay time is mainly determined by the recombination. Simulations show that for InGaN QWs with typical diffusion coefficients in the 0.1 cm^2/s to 1 cm^2/s range[22,41,42] this criterion is satisfied for carrier lifetimes below 1 ns.[22] However, if the carrier lifetimes are longer and the diffusion length exceeds the probe aperture, the ambipolar diffusion becomes dominant.

To resolve whether the near-field PL decay times are determined by the nonradiative recombination or diffusion, SNOM measurements were repeated using a large aperture (400 nm) probe, and in the far field with an excitation spot diameter of 50 μm. The far-field PL decay times vary from 23 ns for the violet to 153 ns for the green-yellow QW (Table II). These values exceed the small aperture near-field PL decay times by one to two orders of magnitude (Figs. 2–4, Table II). For the large aperture SNOM measurements, the average PL decay times are in the intermediate range (Table II), still considerably smaller than those measured in the far field. Apart from this, there are two more observations that are important when discussing mechanisms of the near-field PL decay. The first one is the spatial variation of the near-field PL decay time within a particular sample. As the measurement data show (Figs. 2–4, Table I), the decay times are significantly shorter in the defect-rich compared to the defect-free regions. The second one is the fact that the small aperture PL decay times are similar for all samples, while the far-field times vary strongly (Table II) and depend on the QW depth and FWHM.

Let us look into the PL decay times in the defect-poor and defect-rich regions of the QWs. Here, the defect-poor regions are defined as the ones that are separated from the dislocations and V-defects by more than one diffusion length. In those areas, the PL decay time is determined by the radiative recombination and non-radiative Shockley–Read–Hall recombination via deep recombination centers formed by impurities and point defects. The large difference between the near-field and far-field PL decay times shows that in the defect-free areas the near-field PL decay is determined by the carrier out-diffusion from under the probe. This is also valid for the large aperture case showing that the diffusion length exceeds the large aperture radius of 200 nm.

On the other hand, in the vicinity of the V-defects, the small aperture PL decay times are short, about 1–2 ns. This local decrease of the PL decay time can either be determined by a faster carrier out-diffusion from under the probe or by a faster nonradiative recombination. Here, one should recall that the defect-rich areas have broader spectra, i.e., deeper localization potentials. Taking into account that the ambipolar diffusion is limited by the thermally assisted hopping of holes between localized states,[43] one would expect that in the defect-rich regions the diffusion would be slower. Thus, if the near-field PL decay were determined by the diffusion, in the defect-rich regions the PL decay times would be longer than in the defect-free areas, which contradicts the experimental data. Consequently, the short near-field PL decay times in the defect-rich regions should be assigned to the nonradiative recombination. This enhanced recombination would take place at dislocations and/or point defects that decorate the dislocations. The latter have previously been identified as an important channel of the nonradiative recombination in GaN.[44]

In the defect-rich regions, the near-field PL decay times are similar for all samples and do not experience any significant dependence on the QW depth. This suggests a similar origin of the nonradiative recombination centers for all QWs. In the defect-free regions, in which the PL decay is determined by the carrier out-diffusion from under the probe, different well depth dependencies are observed for the small and large aperture decay times. For the small aperture measurements, the PL decay times are very similar for all samples. For the large aperture measurements, the decay time increases as the In content in the QW is increased (Table II). These dependencies can be understood by taking into account that the small aperture out-diffusion time takes place at the initial period of the diffusion process characterized by higher carrier densities and higher diffusion velocity.[22] In this regime, the carrier localization plays a minor role. For larger diffusion distances probed by the large aperture probe, the diffusion slows down and is more affected by the carrier localization. Consequently, the out-diffusion times become longer for high In content QWs with deeper localization potentials. This is in agreement with the alloy composition dependence of the diffusion coefficient in InGaN QWs.[41,42]

The large difference between the short near-field PL decay times, determined by the nonradiative recombination, and the far-field PL decay times shows that areas that are affected by the nonradiative recombination at dislocations and V-defects occupy just a small fraction of the QWs. For the green-yellow QW, the near-field PL decay time in the defect-rich regions is more than two orders of magnitude shorter than the far-field PL decay time. Consequently, the dislocation-related nonradiative recombination takes place in about 1% of the sample area. For the V-defect density of $2 \times 10^8\,\mathrm{cm}^{-2}$ and an average V-defect area of $1.3 \times 10^{-10}\,\mathrm{cm}^2$ (the same for all samples), the V-defects occupy ∼3% of the sample area. This is larger than the area affected by the nonradiative recombination at dislocations. This means that for the high In content QWs carriers should be excited directly into the dislocations for the fast nonradiative recombination to occur. Otherwise, this recombination is hindered, either by the V-defect potential barriers or by the efficient carrier localization. For the short wavelength QWs, the ratio between the time of the nonradiative recombination at dislocations and the far-field PL decay time is smaller, ∼20 for the violet and ∼50 for the blue QW. Apparently, for these structures, the potential barriers or the localization potentials are less effective in preventing the nonradiative recombination at dislocations. Nevertheless, this process is still local without a major impact on the overall, spatially integrated nonradiative recombination.

V. CONCLUSIONS

Spectrally- and time-resolved scanning near-field optical microscopy was applied to study spatial variations of PL spectra and carrier dynamics in polar InGaN/GaN QWs emitting in a broad spectral range, from 410 nm to 570 nm. The PL intensity, peak wavelength, and linewidth, as well as the radiative and nonradiative recombination times, were found to be different in V-defect-rich and defect-free regions. The radiative lifetime close to the defects was enhanced up to several times, which is attributed to an increased electron and hole wave function separation in the QW plane. This increased separation is assigned to larger In content and band potential variations in the vicinity of V-defects, as evidenced by the EDS. Variations of the lateral wave function separation dominate the radiative lifetime distribution within the same QW; for QWs with different alloy compositions, the vertical wave function separation induced by the piezoelectric field plays the main role. The PL decay time measured in the near-field I–C mode was found to be much shorter than the decay time measured in the far field. Comparison of the PL decay times measured in different experimental configurations shows that the near-field PL dynamics and the integrated PL intensity are primarily determined by the carrier out-diffusion from under the probe. Only in the immediate vicinity of the V-defects does the near-field PL decay due to the nonradiative recombination at the dislocations. The area of such enhanced nonradiative recombination is limited to just a few percent of the total QW area. This shows that recombination via dislocations and V-defects does not play a decisive role in the overall nonradiative recombination and internal quantum efficiency of polar InGaN/GaN QWs.

ACKNOWLEDGMENTS

The research at KTH has been financially supported by the Swedish Research Council (Contract No. 45390-1) and the Swedish Energy Agency (Contract No. 2018-04783). The work at UCSB was supported by the U.S. Department of Energy under Award No. DE-EE0008204, the National Science Foundation under Award No. 1839077, and the Simons Foundation through Grant No. 601952.

DATA AVAILABILITY

The data that support the findings of this study are available from the corresponding author upon reasonable request.

REFERENCES

[1] C. Weisbuch, ECS J. Solid State Sci. Technol. **9**, 016022 (2020).
[2] W. Hahn, J.-M. Lentali, P. Polovodov, N. Young, S. Nakamura, J. S. Speck, C. Weisbuch, M. Filoche, Y.-R. Wu, M. Piccardo, F. Maroun, L. Martinelli, Y. Lassailly, and J. Peretti, Phys. Rev. B **98**, 045305 (2018).
[3] D. Watson-Parris, M. J. Godfrey, P. Dawson, R. A. Oliver, M. J. Galtrey, M. J. Kappers, and C. J. Humphreys, Phys. Rev. B **83**, 115321 (2011).
[4] T. K. Uždavinys, D. L. Becerra, R. Ivanov, S. Nakamura, S. P. DenBaars, J. S. Speck, and S. Marcinkevičius, Opt. Mater. Express **7**, 3116 (2017).
[5] A. Hangleiter, F. Hitzel, C. Netzel, D. Fuhrmann, U. Rossow, G. Ade, and P. Hinze, Phys. Rev. Lett. **95**, 127402 (2005).
[6] X. H. Wu, C. R. Elsass, A. Abare, M. Mack, S. Keller, P. M. Petroff, S. P. DenBaars, J. S. Speck, and S. J. Rosner, Appl. Phys. Lett. **72**, 692 (1998).
[7] Z. Quan, L. Wang, C. Zheng, J. Liu, and F. Jiang, J. Appl. Phys. **116**, 183107 (2014).
[8] I.-H. Kim, H.-S. Park, Y.-J. Park, and T. Kim, Appl. Phys. Lett. **73**, 1634 (1998).
[9] X. Jiang, C. Zheng, C. Mo, X. Wang, J. Zhang, Z. Quan, J. Liu, and F. Jiang, Opt. Mater. **89**, 505 (2019).
[10] T. L. Song, J. Appl. Phys. **98**, 084906 (2005).
[11] M. H. Zoellner, G. A. Chahine, L. Lahourcade, C. Mounir, C. L. Manganelli, T. U. Schülli, U. T. Schwarz, R. Zeisel, and T. Schroeder, ACS Appl. Mater. Interfaces **11**, 22834 (2019).
[12] M.-H. Sheen, S.-D. Kim, J.-H. Lee, J.-I. Shim, and Y.-W. Kim, J. Electron. Mater. **44**, 4134 (2015).

[13] I. A. Ajia, P. R. Edwards, Y. Pak, E. Belekov, M. A. Roldan, N. Wei, Z. Liu, R. W. Martin, and I. S. Roqan, ACS Photonics **5**, 820 (2018).
[14] S. Kurai, S. Higaki, N. Imura, K. Okawa, R. Makio, N. Okada, K. Tadatomo, and Y. Yamada, Phys. Status Solidi B **255**, 1700358 (2018).
[15] M. Liu, J. Zhao, S. Zhou, Y. Gao, J. Hu, X. Liu, and X. Ding, Nanomaterials **8**, 450 (2018).
[16] T. Shin, X.-S. Li, D.-S. Ko, J.-Y. Won, S.-H. Kim, J. Kim, J. Kim, Y. Tak, J.-Y. Kim, G.-S. Park, and E. Lee, Chem. Phys. **436-437**, 51 (2014).
[17] A. Kaneta, M. Funato, and Y. Kawakami, Phys. Rev. B **78**, 125317 (2008).
[18] S. Marcinkevičius, Y. Zhao, K. M. Kelchner, S. Nakamura, S. P. DenBaars and J. S. Speck, Appl. Phys. Lett. **103**, 131116 (2013).
[19] N. Okada, H. Kashihara, K. Sugimoto, Y. Yamada, and K. Tadatomo, J. Appl. Phys. **117**, 025708 (2015).
[20] S. Kurai, K. Okawa, R. Makio, G. Nobata, J. Gao, K. Sugimoto, N. Okada, K. Tadatomo, and Y. Yamada, J. Appl. Phys. **124**, 083107 (2018).
[21] Y. Li, W. Tang, Y. Zhang, M. Guo, Q. Li, X. Su, A. Li, and F. Yun, Nanomaterials **9**, 633 (2019).
[22] M. Mensi, R. Ivanov, T. K. Uždavinys, K. M. Kelchner, S. Nakamura, S. P. DenBaars, J. S. Speck, and S. Marcinkevičius, ACS Photonics **5**, 528 (2018).
[23] O. Brandt, H. Yang, and K. H. Ploog, Phys. Rev. B **54**, R5215 (1996).
[24] R. Ivanov, S. Marcinkevičius, T. K. Uždavinys, L. Y. Kuritzky, S. Nakamura, and J. S. Speck, Appl. Phys. Lett. **110**, 031109 (2017).
[25] S. Marcinkevičius, K. M. Kelchner, L. Y. Kuritzky, S. Nakamura, S. P. DenBaars, and J. S. Speck, Appl. Phys. Lett. **103**, 111107 (2013).
[26] V. Fiorentini, F. Bernardini, F. Della Sala, A. Di Carlo, and P. Lugli, Phys. Rev. B **60**, 8849 (1999).
[27] D. S. P. Tanner, M. A. Caro, E. P. O'Reilly, and S. Schulz, RSC Adv. **6**, 64513 (2016).
[28] R. Ivanov, S. Marcinkevičius, Y. Zhao, D. L. Becerra, S. Nakamura, S. P. DenBaars, and J. S. Speck, Appl. Phys. Lett. **107**, 211109 (2015).
[29] S. Marcinkevičius, T. K. Uždavinys, H. M. Foronda, D. A. Cohen, C. Weisbuch, and J. S. Speck, Phys. Rev. B **94**, 235205 (2016).
[30] M. Takeguchi, M. R. McCartney, and D. J. Smith, Appl. Phys. Lett. **84**, 2103 (2004).
[31] F. Bernardini and V. Fiorentini, Appl. Surf. Sci. **166**, 23 (2000).
[32] F. C.-P. Massabuau, P. Chen, M. K. Horton, S. L. Rhode, C. X. Ren, T. J. O'Hanlon, A. Kovács, M. J. Kappers, C. J. Humphreys, R. E. Dunin-Borkowski, and R. A. Oliver, J. Appl. Phys. **121**, 013104 (2017).
[33] D. F. Feezell, J. S. Speck, S. P. DenBaars, and S. Nakamura, J. Disp. Technol. **9**, 190 (2013).
[34] W. G. Scheibenzuber, U. T. Schwarz, R. G. Veprek, B. Witzigmann, and A. Hangleiter, Phys. Rev. B **80**, 115320 (2009).
[35] S. Tomiya, Y. Kanitani, S. Tanaka, T. Ohkubo, and K. Hono, Appl. Phys. Lett. **98**, 181904 (2011).
[36] C. Netzel, H. Bremers, L. Hoffmann, D. Fuhrmann, U. Rossow, and A. Hangleiter, Phys. Rev. B **76**, 155322 (2007).
[37] M. Piccardo, C.-K. Li, Y-R Wu, J S. Speck, B. Bonef, R. M. Farrell, M. Filoche, L. Martinelli, J. Peretti, and C. Weisbuch, Phys. Rev. B **95**, 144205 (2017).
[38] V. Liuolia, A. Pinos, S. Marcinkevičius, Y.-D. Lin, H. Ohta, S. P. DenBaars and S. Nakamura, Appl. Phys. Lett. **97**, 151106 (2010).
[39] R. Butté, L. Lahourcade, T. K. Uždavinys, G. Callsen, M. Mensi, M. Glauser, G. Rossbach, D. Martin, J.-F. Carlin, S. Marcinkevičius, and N. Grandjean, Appl. Phys. Lett. **112**, 032106 (2018).
[40] C. Mounir, U. T. Schwarz, I. L. Koslow, M. Kneissl, T. Wernicke, T. Schimpke, and M. Strassburg, Phys. Rev. B **93**, 235314 (2016).
[41] R. Aleksiejūnas, K. Nomeika, S. Miasojedovas, S. Nargelas, T. Malinauskas, K. Jarašiūnas, Ö. Tuna, and M. Heuken, Phys. Status Solidi B **252**, 977 (2015).
[42] J. Danhof, H.-M. Solowan, U. T. Schwarz, A. Kaneta, Y. Kawakami, D. Schiavon, T. Meyer, and M. Peter, Phys. Status Solidi B **249**, 480 (2012).
[43] K. Kazlauskas, G. Tamulaitis, P. Pobedinskas, A. Žukauskas, M. Springis, C. F. Huang, Y. C. Cheng, and C. C. Yang, Phys. Rev. B **71**, 085306 (2005).
[44] D. C. Look and J. R. Sizelove, Phys. Rev. Lett. **82**, 1237 (1999).